Synchronized Eruptions on Io: Possible Evidence of Interconnected Subsurface Magma Reservoirs

A. Mura[1*], R. Lopes[2], F. Nimmo[3], S. Bolton[4], A. Ermakov[5], J. T. Keane[2], F. Tosi[1], F. Zambon[1], R. Sordini[1], J. Radebaugh[6], J. Rathbun[7], W. McKinnon[8], S. Goossens[9], M. Paris[1], M. Mirino[1], A. Cicchetti[1], G. Piccioni[1], R. Noschese[1], G. Sindoni[10], C. Plainaki[10]

[1] Institute for Space Astrophysics and Planetology, National Institute for Astrophysics (IAPS/INAF), Rome, Italy

[2] Jet Propulsion Laboratory, California Institute of Technology, Pasadena, CA, USA

[3] Department of Earth and Planetary Sciences, University of California, Santa Cruz, Santa Cruz, CA, USA

[4] Southwest Research Institute, San Antonio, TX, USA

[5] Department of Aeronautics and Astronautics, Stanford University, Stanford, CA, USA

[6] Brigham Young University, Provo, UT, USA

[7] Cornell University, Ithaca, NY, USA

[8] Department of Earth, Environmental, and Planetary Sciences, Washington University in St. Louis, St. Louis, MO, USA

[9] NASA Goddard Space Flight Center, Greenbelt, MD, USA

[10] Agenzia Spaziale Italiana, Rome, Italy

Abstract. On December 27, 2024, Juno's JIRAM (Jovian InfraRed Auroral Mapper) instrument observed an unprecedented volcanic event on Io's southern hemisphere, covering a vast region of ~ 65,000 km², near 73°S, 140°E. Within the imaged region, only one hot spot was previously known (Pfd454). This feature was earlier estimated to cover an area of 300 km² with a total power output of 34 GW. JIRAM results show that the region produces a power output of 140 - 260 TW, over 1,000 times higher than earlier estimates and likely exceeding the brightest eruption ever recorded on Io, that of Surt in 2001 (~80 TW). Three adjacent hot spots also exhibited dramatic power increases: P139, PV18, and an unnamed feature south of the main one that surged to ~1 TW, placing all of them among the top 10 most powerful hot spots observed on Io. A temperature analysis of the features supports a simultaneous onset of these brightenings and suggests a single eruptive event propagating beneath the surface across hundreds of kilometers, the first time this has been observed on Io. This in turn would imply a connection among the hotspots' magma reservoirs, while other nearby hotspots that have been known to be active in the recent past, such as Kurdalagon Patera, appear unaffected. The simultaneity supports models of massive, interconnected magma reservoirs. The topology of these regional magma systems may resemble that of an large-scale sponge, in which the massive reservoirs are the pores, interconnected through a largely solid outer shell.

Plain Language Summary. On December 27, 2024, NASA's Juno spacecraft observed an enormous volcanic eruption on Io, Jupiter's most volcanically active moon. The eruption covered a vast area of about 65,000 km² in the southern hemisphere and released an estimated 140-260 terawatts of energy-possibly the most intense volcanic event ever recorded on Io, far surpassing previous eruptions.

The eruption affected multiple volcanic hot spots, with some increasing in brightness by over 1,000 times their usual levels. Scientists believe this was a single, massive event spreading underground across hundreds of kilometers, linking multiple magma reservoirs. However, other nearby volcanoes remained unaffected, adding complexity to how Io's interior works.

This unprecedented event suggests that Io's volcanoes may be more interconnected than previously thought. Future observations by Juno could reveal whether the eruption left behind new lava flows or ash deposits, helping scientists better understand the moon's geology and volcanic activity.

Introduction

Much of the surface of Io, the most volcanic world in our solar system, is dominated by vast lava flows and paterae. Paterae are volcanic depressions resembling terrestrial calderas but often significantly larger (Carr et al., 1998; McEwen et al., 2000); however, their formation mechanism is unlikely to be the same as on Earth (Radebaugh et al., 2001). While it is clear that Io's paterae are surface expressions of subsurface magma intrusion processes, with various models proposed (such as Keszthelyi et al., 2004, and Radebaugh et al., 2004), there is little definitive knowledge of the pathways and mechanisms by which magma generated in Io's tidally-heated mantle ascends through the crust. Another unresolved question is the extent to which Io’s heat is transported to the surface through conduction versus advection through high-temperature hotspots (McEwen et al., 2023). Io operates via a heat-pipe volcanic cycle, in which surface eruptions and subsurface intrusions act to drive the moon’s lithosphere inward, suppressing outward heat flow from depth except through magmatic conduits (e.g., Spencer et al., 2020). Heat-pipe volcanism puts the deeper portion of the lithosphere into compression, plausibly explaining Io’s global distribution of tall, tectonic mountains (O’Reilly and Davies, 1981). This is in conflict with the persistence of Io’s continual volcanic eruptions, as compression acts to close off volcanic conduits and limit eruptions. Thrust faulting and mountain formation, however, relieves these compressional stresses and can actually drive the surface lithosphere into extension, both of which can promote volcanic eruptions (Bland and McKinnon, 2016). Juno Stellar Reference Unit (SRU) images (Becker et al. 2025) are suggestive of recent volcanic activity influenced by tectonics.

The relative contributions of surface eruptions versus subsurface intrusions (i.e., pluton formation or lateral incursion into the crust through sills) is unknown, and the interplay between Io’s prodigious volcanic output and its tectonic (i.e., non-volcanic) mountain building is poorly understood (Schenk et al. 2001; Turtle et al. 2001; Jaeger et al. 2003). Understanding how much heat is transported via conduction or advection is crucial for modeling Io’s global heat flow and regional thermal patterns and understanding its volcano-tectonic system. The advectively transported heat could originate from cooling surface or near-surface lava flows and/or from exposed lava, such as in lava lakes (Lopes et al. 2004, Mura et al. 2025a). Observational evidence, such as the presence of numerous caldera-like depressions and long-duration eruptions like those at Prometheus, points to the existence of subsurface reservoirs or magma chambers (Leone et al., 2009; Hamilton et al. 2013).

Io offers critical insights into tidal heating, one of the primary drivers of geological activity in our solar system and beyond. Recent measurements of Io’s tidal response (Park et al. 2025) indicate that while the existence of a deep magma ocean cannot be ruled out, a shallow globally molten layer could not be the source of Io’s volcanism. Instead, localized subsurface reservoirs, whose connectivity is not well understood, may better describe the source of Io’s volcanic activity. Investigating the characteristics of Io’s magma chambers and transport systems, as well as monitoring Io’s volcanic activity and determining recharge times and eruption intervals, is essential to advance our understanding of this enigmatic moon.

Observations and results

On December 27, 2024, between 00:43 UTC and 01:56 UTC, the JIRAM (Jovian InfraRed Auroral Mapper) experiment on board Juno (Adriani et al., 2017; Mura et al., 2018) observed the southern hemisphere of Io, initially from a distance of 100,000 km, decreasing to 75,000 km over about one hour, achieving a spatial resolution from 23 to 17 km. The time interval mentioned is simply a result of the observation geometry, as JIRAM's Field of View is constrained and cannot be directed arbitrarily. The instrument, equipped with a dual-band imager (L band: ~3.3 to 3.6 µm; M band: ~4.5 to 5 µm) and a spectrometer channel (2 to 5 µm, well suited for detecting the temperatures associated with the event) detected an event of extreme infrared radiance over a vast region centered at 73°S, 140°E, south and east of Nemea Planum, Crimea Mons and Olafat Patera, west of Illyrikon Regio (Figure 1, feature "A"). Such intense radiance observed by JIRAM comes from a region that covers an area of approximately 65,000 km² on Io's surface, spanning more than 200 km in latitude and more than 400 km in longitude. The radiance is so strong that it produced considerable saturation on the detector. Detached regions of similarly intense radiation, likely associated with the same event (based on thermal analysis as described in the "Methods" section), were also detected, with very high radiance as well. A very large feature ("B" in Figure 1) lies just south of the most intense feature ("A" in Figure 1). As seen in Figure 1, panel D, feature "A" could indeed consist of two distinct features, one to the east and one to the west (either would be remarkably large, a point we will return to below). The signal maintained its extreme intensity throughout the observation period, suggesting the event likely persisted both before and after the observation window. This region lacked substantial thermal emission only two months earlier (orbit 66, Figure 1 panel B.). Furthermore, available images do not reveal a clear preexisting patera at this location (“A”), only previous long lava flows, though the image resolution in that region is poor.

Analyzing fully saturated images is challenging; however, the spectrometer has been used to retrieve the total power of the feature; also, the signal's strength caused a distinctive stray-light feature, attributable to the same source, to be detected in a different region of the detector

(Figure 2), which is not saturated and it is used to retrieve the radiance of the saturated data (see "Methods").

Based on the analysis performed with both the spectrometer and the imager, the total power from the main feature ranges from 140 to 260 TW, making this event likely the most intense ever recorded on Io, likely exceeding the prior brightest event, which was observed at Surt in 2001 (~80 TW) (Marchis et al., 2002).

What makes this event truly remarkable is the vast extent of the surface area involved. As noted, the main feature spans approximately 65,000 km^2 (see "Methods"), being three times as large as Loki Patera (~20,000 km^2), known as the largest active volcanic patera on Io (typically emitting ~10–20 TW; Rathbun et al., 2004; de Kleer and de Pater, 2017). Within the observed region, there is one feature previously identified as a dark patera by Williams et al. (2011) located at 74.7°S, 134.4°E and designated Pfd454. Veeder et al. (2012) calculated from the Williams et al. (2011) map that the area of Pfd454 is 300 km^2, more than two orders of magnitude smaller than the size of the current eruption. Given the sheer size of the main spot observed now, it cannot be conclusively attributed to Pfd454, as it may be a newer hotspot that has swallowed Pfd454. However, comparisons to Pfd454 are still useful since they give information about the historical power output in this region. Veeder et al. (2012) used an average hotspot temperature to estimate the power of this feature to be 34 GW. We also reanalyzed PPR data and found that the power of Pfd454 is within a factor of two of 0.1 TW (see "Methods" in the Appendix). Notably, the total power detected by JIRAM is greater by more than a factor of 1,000 than either the estimated or measured value of Pfd454 before the outburst began, highlighting the remarkable intensity of this event at a geological site previously not expected to host such a bright eruption.

Of equal, if not greater, importance is the dramatic increase in power output observed at several hot spots near the main feature ("A"). Table 1 provides a summary of the total power for different features discussed here, together with previous estimations (see "Methods" for details on the calculation). Specifically, the unnamed hot spot to the south ("B"), the Illyrikon A spot, and two hot spots to the north (PV18 and P139) have exhibited remarkable power output increases. Feature B was not previously reported and was completely dark in PJ66. In PJ66 Illyrikon A was measured to have a total power of 1.5 GW, and emitted 50 GW during the event in this study. P139 and PV18 had previously measured power outputs of <80 GW and ~90 GW, respectively (the latter value is from Veeder et al., 2015), but in the JIRAM PJ68 observations both had enormous power outputs of more than 1 TW (see "Methods"). Given that these hot spots are located between 200 and 400 km from the main hot spot in different directions and given that previous surveys (Mura et al., 2024a) reported no such drastic power output variations, it is reasonable to assume that these events, and hence the hotspots, are geologically coupled or connected in some manner. Based on data from Mura et al., 2024b, even the probability of having five nearby hotspots increasing their power output by a factor of only 10 by chance can be calculated as negligible. On the other hand, several other distal hotspots, such as Kurdalagon Patera, exhibited the same radiance one month before (PJ66, see Figure 1 – panel B), or no radiance observed at all (P137) suggesting that this phenomenon is confined within a finite perimeter. A temperature analysis of Feature A, Feature B, PV18, and P139 (see Table 1) suggests that all their temperatures are similar (between 500 and 600 K); this could be explained if the different brightenings began simultaneously, about one day before the observation if we apply the model by de Kleer and de Pater (2017, their figure 1). The model by Mura et al. (2025b), which includes finite lava sheet thickness, yields similar results. Illyrikon A shows a higher temperature, suggestive of an even more recent outburst of lava.

Discussion

We have observed brightening of multiple hot spots over timescales < 1 month and over an area of radius of ~200-400 km. While a detailed interpretation of this (near-) simultaneity is beyond the scope of this paper, we offer some preliminary suggestions here.

One possible interpretation is that the eruptions are originated from a magma chamber or reservoir that fed individual eruption sites via a network of sills and dykes, analogous to – but at a larger scale than – that inferred to exist beneath the main island of Hawai'i (Wilding et al. 2023). Hamilton et al. (2013) previously proposed interactions between Io’s volcanic centers based on their surface distributions. If the eruptions are triggered by melt transport, then the lower bound on the melt velocity required is of order 0.3 km/h, comparable to dike propagation rates inferred at Iceland (Eibl et al. 2017). Other forms of triggering − such as propagation of elastic stresses arising from deformation (Karlstrom et al. 2009, Montagna & Gonnermann 2013, Biggs et al. 2016) or tides (de Kleer et al. 2019a) − would be effectively instantaneous. We suggest that a single interconnected reservoir or magmatic plumbing system underlies multiple hotspots and that during this time, a single large event caused magma in that reservoir to flow or spill simultaneously over into these interconnected near-surface source regions, manifest as hotspots, possibly triggered by pressure changes in the deeper feeder reservoir, by a dramatic magma surge from depth, or by substantial tectonic activity causing a roof collapse or other major faulting event. This model does not require access to a global magma ocean, but can instead be explained by an extensive regional magma reservoir or magmatic plumbing system of significant size. Thus, the model is consistent with the interior model based on Juno gravity data proposed by Park et al. (2025), which indicates that Io does not have a shallow global magma ocean. Specifically, the total heat flow out of Io appears to be carried from deeper levels in a partially molten region of global extent (as magmatic activity is global), but at less than the critical melt fraction for disaggregation (which would result in a suspension instead of a partial melt). Channeling of that melt toward discrete eruptive centers ("heat pipes") implies the formation of (possibly shallow) magma lakes or reservoirs beneath or within Io's cold shell, because the critical melt fraction for disaggregation is necessarily exceeded as that melt flow is focused.

On Earth, deep-seated pulses of magma can lead to subsequent volcanic eruptions, similar to the "surge" documented beneath Hawai'i (Poland et al., 2012). A similar process, albeit on a different timescale, may be at play within Io, where a deeper magma reservoir could have supplied material to several shallow chambers or reservoirs, resulting in simultaneous or near-simultaneous eruptions. A sketch of this process is provided in Figure 4. The size of the implied deep magma reservoir could significantly exceed that of its terrestrial counterparts, likely due to the higher heat flow, lower gravity and rigid lithospheric lid of Io. Eruption rates inferred from the thermal power output of ~200 TW correspond to approximately 0.2 km^3/hour of material erupting and cooling through 1000 K. Assuming the eruption lasted many days (we have evidence that the event was still ongoing 4 months later, see figure 1 panels E and F; see also Appendix A3), the total erupted volume could be on the order of 100 km^3. Such a large volume is still insufficient to induce substantial subsidence and tectonic deformation of a hypothetical 100 by 100 km wide magma chamber (the size of the main feature we observed). These eruption rates are comparable to those inferred for large igneous provinces (LIPs) on Earth (Biasi and Karlstrom 2021), while the total volume is somewhat smaller (Reidel et al. 2013). To estimate the necessary dimensions of a dike capable of sustaining a magma flow rate of 0.2 km^3/hour, we consider a 100 km-long dike, which corresponds to a flow rate of approximately 0.5 m^2/s per unit length. Assuming a lava viscosity of 100 Pa·s, a dike width of about 2 meters would be sufficient to accommodate this flux; such a width is comparable to the mean value found in flood basalts on Earth (Karlstrom et al. 2017). This relatively small width suggests that magma supply rates are unlikely to be a limiting factor. Sills are also invoked by the model by Keszthelyi et al. (2004), where mafic magma rising through Io's crust accumulates beneath a near-surface layer of frozen volatiles, forming a horizontal magma sheet (i.e. a sill), which eventually leads to the collapse of the roof and the formation of a new patera.

The observations by Mura et al. (2024b, 2025a) show that many hot spots on the surface of Io have ring-shaped thermal signatures, suggesting that these are lava lakes. The central parts of these lakes are covered by crust, and only the lava close to the patera's walls is exposed—due to abrasion—and emitting heat. In the case of a violent eruption at such a lake, we would expect the crust to break apart, followed by the slow cooling of new crust and the formation of a brighter new 'ring-shaped' thermal signature. This is in fact what we observe for P139 (Figure 3, panel B) if we stretch the color scale with respect to Figure 1: the ring-shaped emission is visible, but it is much less pronounced compared to the many other lava lakes described by Mura et al. (2025a), suggesting that the feature is newly formed. Stretching the color scale for Feature B (in Figure 3 panel C) shows something similar: it appears to be a lava lake with an outflow going to the west. This implies that the event either triggered some changes in the equilibrium of pre-existing lava lakes (such as P139) or created new ones (Feature B), causing lava to spill out. Figure 4 shows a sketch of the proposed model. Evidence for other past overflow events can be seen in cooled lava flows surrounding many other paterae across Io, including Loki.

The extent and irregular outline of Feature A is consistent with massive spillover from a patera or another eruptive center such as a fissure. If the triggering event was indeed formation or collapse of a new or pre-existing (but previously unrecognized) patera or series of paterae, crustal decompression, propagated laterally, could have facilitated magma ascent elsewhere, possibly involving exsolution of (given Io's volcanic chemistry) magmatic sulfur and sulfur oxides (cf. Montagna and Gonnermann 2013). In addition, Io's heat-pipe engine nominally leads to widespread crustal compression, which acts to inhibit volcanism (and exsolution of volatiles). Therefore, major tectonic thrust events (such as involved in mountain formation) could relieve these stresses regionally and also lead to favorable stress conditions for volcanic eruptions, both from pre-existing paterae and along the thrust faults themselves (Bland and McKinnon 2016). Given the measured gravitational response of Io to tidal forcing (Park et al. 2025), tidal stress changes are only on the order of 0.1 MPa, and are less likely, in and of themselves, to trigger a major eruption.

Conclusion

We have observed a large volcanic outburst on Io, with the most intense power output ever recorded. Several other large eruptions that occurred simultaneously nearby have revealed, for the first time, the structure and vast extent of the connections between different paterae on Io: a system of apparently interconnected magma reservoirs situated hundreds of kilometers from each other. The details of this system, and how triggering occurred, are still unclear; for instance, are individual shallow reservoirs connected by discrete dykes to a larger chamber at depth, or are they a large-scale manifestation of partially-molten material (a "sponge"; de Kleer et al. 2019b)? An extensive subsurface magma system on Io would help to explain the observations of globally distributed lava lakes (Mura et al., 2025a), where the lake surfaces are thought to move vertically. If there were regional connections between paterae, they might all respond together and similarly to forcing from a large magma source.

An eruption of this magnitude is likely to leave a long-lived signature. Previous large eruptions at Io have left varied features such as a large area thought to be pyroclastic deposits (Pillan patera eruption in 1997, see McEwen et al. 1998), large red sulfur rings, or small, maybe fissure-fed lava flows (Tvashtar in 1999, see Turtle et al. 2004 and Thor in 2001, see Lopes et al., 2004). Surface changes resulting from the eruption, and the temporal evolution of the event, can be further studied with upcoming data from Juno.

Our observations support the emerging picture of extensive regional magma systems on Io rather than volcanism being sourced from a globally magma ocean (cf. Park et al. 2025). The topology of these regional magma systems may in some ways resemble that of an enormous sponge. In this model, discrete, large subsurface reservoirs are the pores, interconnected through a largely solid outer shell. Future observations by Juno may clarify the late 2024 eruptive event's nature, which could have left pyroclastic deposits or lava flows akin to previous large eruptions, offering insights into Io's volcanic and tectonic regimes. Earth-based observations of this region may also be possible, although the observational geometry is extremely limited owing to the region's high latitude. Remaining questions about changes from this eruption and the interconnectedness of magma in Io's interior may not be answerable in detail without future exploration.

Appendix

A1. Methods

A.1.1 Imager data

To calculate the total power emitted from a feature, we need at least the dual-band (L and M, respectively 3.45 μm and 4.8 μm) spectral output, following the method by Mura et al. (2024a); in fact, Tosi et al. (2025) demonstrated that the fraction of the total power in a single band is highly variable due to temperature variability.

To retrieve the radiance within the saturated region (which evidently dominates the signal) a well-defined stray-light feature is used (visible in Appendix Figure A1). This feature is caused by reflection of light inside the instrument, and it is a stable feature. It is present in all JIRAM imager data, and being much less intense than the primary signal, it is usually barely visible. In Appendix Figure A2, we present four example images from PJ6, where the stray-light feature is evident due to the very long exposure time used (330 ms); the feature is highlighted in the red rectangles, and Io – the main target and signal – is inside the white circle. The rectangle measures ~45 × 20 pixels and is located ~50 pixels above the main feature (Io); as it appears from the images, the location is very stable relative to the main feature. The intensity of the signal from Io in the M band has been automatically calculated, and the average radiances inside both the circle (radius of 8 pixels, corresponding to Io) and the rectangle are estimated. This procedure is repeated for all 99 images taken during orbit 6, during which the signal did not saturate the detector, even though the signal was intense (peaking at approximately 10,000 DN). For the M band, the mean ratio of the signal to stray light (f) is found to be:

$$f = 400 \pm 100 \tag{1}$$

Here and in the following, the uncertainty is estimated as twice the standard deviation (2σ). We then analyze the images taken during the eruption, shown in Appendix Figure A3. The average spectral radiance in the rectangle is measured to be R = 200 ± 60 mW m^{-2} sr^{-1} μm^{-1}; using the average spectral radiance R and scaling by the factor f we obtain R' = 78 ± 25 $W \cdot m^{-2} \cdot sr^{-1}$ μm^{-1}. The area (A) that corresponds to the red circle in figure A3 is approximately 80 10^3 km^2, leading to a total M-band power P_M of:

$$P_M = R \cdot f \cdot A \cdot \pi = 19 \pm 8 \text{ TW } \mu m^{-1}. \tag{2}$$

To evaluate the uncertainty of this estimation, we note that P_M also depends on the factor f; we therefore add the relative error of f (~20%) to the relative error of $R \cdot A$ (~20%); the total uncertainty is approximately 40%, yielding the 8 TW μm^{-1} uncertainty in the above formula. Appendix Table A1 provides the data used for this calculation; times are given in Coordinated Universal Time (UTC).

A similar calculation is performed for the L band. In this case, the factor f is different, because the stray light is dispersed before the filters, and each filter has a different transparency:

$$f = 125 \pm 16; \tag{3}$$

and performing a similar calculation as for the M band gives a value of P_L of approximately:

$$P_L = 8.9 \pm 2.5 \text{ TW } \mu m^{-1}. \tag{4}$$

Also in this case, we add the relative errors of the measure of f and of the measure of $R \cdot A$ to obtain the relative error on P_L. Table A2 provides the data used for this calculation.

A.1.2 Spectrometer Analysis

The spectrometer provides important support for the analysis. It typically acquires data simultaneously with the imager. Since JIRAM is mounted on a spinning satellite, the spectrometer can work either with a de-spinning mirror, used to stabilize the spectrometer's field of view (FoV) during the exposure, or with fixed pointing, resulting in the integration of the signal along the "line" axis of the imager. In this last mode, the spectrometer can be used to obtain the total power of a hot spot, with a technique that has been introduced in the most recent JIRAM observations and is discussed below. Because the signal was so strong, the spectrometer data coming from Feature A, acquired in PJ68, also exhibit mild saturation, but only at long wavelengths, starting empirically around 3.5 μm. Thus, the L band (~3.3 to 3.6 μm) is practically free of saturation and can be used to validate the measurements presented above, whereas the M band is more saturated and not suitable for this analysis. For the procedure explained in the following, we use spectrometer data from the beginning of the observation, because they show a slightly better quality.

Appendix Figure A3 shows a spectrogram (bottom) an imager frame (top) acquired at the same instant. The imager and spectrometer share part of the FoV; specifically, the spectrometer FoV corresponds to the 13th line of the M filter, covering samples 88 to 344. This overlap was designed to simplify co-localizing the two JIRAM channels. In the figure, Io's bright feature (Feature A) discussed in this study is in the center of the top panel; in the bottom panel, the spectrometer shows a significant signal increase in the corresponding region; other hotspots produce additional vertical streaks (the vertical dimension in the lower panel represents wavelength). Such main feature occupies approximately 16 samples (n_s = 16); we also define n as the number of lines occupied by the feature (this value is approximately 16, but it will be simplified in the calculation, and hence it is not critical).

The exposure time of the spectrometer is T_{exp} = 1 s; the spectrometer's FoV (~238 × 10^{-6} rad, single pixel) rotates with Juno's angular velocity:

$$\omega = \frac{2\pi}{30}\ \mathrm{s}^{-1} \tag{5}$$

The effective exposure time T'_{exp}, during which the spectrometer acquires the signal from the feature is then:

$$T'_{exp} = \frac{n\ iFOV}{\omega} \tag{6}$$

Let R_L be the mean measured band radiance in the L band (~3.3 to 3.6 μm), obtained from the spectrometer and averaged over the n_s samples (0.31 ± 0.08 W m^{-2} sr^{-1} μm^{-1}). The corrected radiance R'_L is hence:

$$R'_L = R_L \frac{T_{exp}}{T'_{exp}} \tag{7}$$

The total power P_L is calculated by multiplying by the subtended area:

$$\begin{aligned} P_L = R'_L\, A\, \pi = R_L \frac{T_{exp}}{T'_{exp}}\, (d^2\, iFOV^2\, n\, n_s)\pi = \\ = R_L \frac{\omega\, T_{exp}}{n\, iFOV}\, (d^2\, iFOV^2\, n\, n_s)\pi = \\ = R_L \omega\, T_{exp}\, d^2\, iFOV\, n_s\, \pi \end{aligned} \tag{8}$$

where d is the observation distance (approximately 90,000 km during the spectrum acquisition on 2024-12-27 at 01:09:45). The result is 6 ± 1.5 TW μm^{-1}; the substantial agreement of this calculation with the previous one (8.9 ± 2.5 TW μm^{-1}) demonstrates the robustness of the estimation of the values of P_L and P_M. The spectrometer-derived estimation is slightly lower than the imager-derived one, and this can be ascribed to i) the fact that while in the imager data the saturation is corrected, a small amount of saturation is still present in the L-band part of the spectrometer, and ii) calibration residuals between the two channels.

A.1.3 Total power and area calculation

The ratio between the M-band spectral power P_M (19 TW μm^{-1}) and the L-band spectral power P_L (8.9 TW μm^{-1}) is indicative of a temperature of ~490 K (note that we use the imager-derived value for P_L , so to be consistent with the value for P_M). At this value, the total power P is a factor 10 or more with respect to the M-band spectral power. That means that the total power can be estimated as ~200 TW. To evaluate the uncertainty, one can redo the same calculation using all combinations of values of P_M and P_L in their respective variability ranges (including the value of P_L = 6 TW μm^{-1} given by the spectrometer and removing all combinations that produce an area larger than the observed one, 65,000 km^2). This will result in the temperature ranging from 450 K to 550 K, and in the total power P ranging from 140 to 260 TW. We conclude that, even with the large uncertainties led by the limits of the measurement, the value of 200 TW is the best estimate for the total power, not counting the features surrounding the main one, and that in any case the total emitted power greatly exceeds the value of 100 TW.

For Pfd454, Veeder et al. (2012) assumed an effective temperature of 211 K, derived from an average of multiple hotspots. This assumption led to a calculated power of 34 GW for Pfd454, which is not a direct measurement but rather an extrapolation based on averaged thermal properties. Veeder et al. (2012) does not give uncertainties in this calculation.

To better estimate the power output and temperature of this feature, we performed a closer analysis of the Galileo PPR data showed in figure 3 of Rathbun et al. (2004). We note a faint warm region near 220° W longitude and -75° latitude, consistent with the location of Pfd454, that was too faint to be noted in Rathbun et al. (2004). Revisiting the original dataset using the same methodology of Rathbun et al. (2004), we estimate a total power of ~0.1 TW for this region. While this value is subject to uncertainties (a factor of ~2) due to the high emission angle (75°), it is substantially higher than the Veeder et al. (2012) estimate. Furthermore, if we assume the area of the feature is that given by Williams (2011), the PPR measured power is consistent with a temperature of 291 +- 30 K.

The area enclosed within the white perimeter shown in Figure 1 is approximately 65,000 km^2. However, it is important to consider that signal saturation in the brightest pixels likely induces bleeding or stray-light artifacts in adjacent ones, potentially leading to some slight overestimation of the actual area.

A.1.4 Total power calculation for the minor features

Four minor features have been identified as emitting considerably more power than in the past observations: PV18, Feature B, P139, Illyrikon A. It is possible to obtain the total power output from either the imager or the spectrometer and, in some cases, from both.

A.1.4.1 PV18

Regarding PV18, the imager data is fully non-saturated in the L band but is slightly saturated in the M band (approximately 35% of the data is saturated, exceeding a 12000 DN threshold, which is the nominal one). We employ the method previously proposed by Pettine et al. (2024) to partially correct the saturated portion by applying a corrective coefficient. Clearly, the M band estimate will still be a lower limit. The total band power is 40 GW μm^{-1} for the L band and 80 GW μm^{-1} for the M band. Using the same procedure described in section 7.3, we obtain a total power of 1 TW and a temperature of 500 K. Considering that the L band is not saturated, and the M band is slightly underestimated, we can suggest that 500 K is slightly overestimated but reasonably close to the true value. It is also important to remember that this temperature is indicative of the equivalent temperature at which a black body emits. Hence, the ratio between the M and L bands is consistent with our observations, but reasonably the temperature within the feature will have a range of values around this mean value. To emit 1 TW at 500 K, an area of about 300 km^2 is needed.

A.1.4.2 Feature B

Feature B can also be analyzed with the imager data, which, however, has a higher saturation (around 50%). The temperature indicated by the M/L ratio is 570 K and is probably more overestimated than that of PV19 for the aforementioned reasons; the spectral power in the L band is 40 GW μm^{-1}, that in the M band is 100 GW μm^{-1}, but remember that it is a saturated value, so certainly an underestimate. In fact, the spectrometer measurements - in this case available and shown in figure 2 panel B - indicate a much greater power, and lead to a temperature estimate T of 550 ± 50 K, lower than the 570 K previously reported. The estimate is obtained with a best fit using a simple two-parameter Markov Chain Monte Carlo (MCMC) model fitting area and temperature. The area is approximately 300 km^2, while the total power P is 1.7 ± 0.2 TW; uncertainties on T and P are 1-σ.

A.1.4.3 Illyrikon A

Illyrikon A can be easily analyzed via the imager data, which is completely free of saturation for this hotspot. The band ratio shows a very high temperature, between 900 and 1000 K, and a small power, around 50 GW.

A.1.4.4 P139

P139 can only be analyzed with the spectrometer, as it saturates the imager channel in both filters. By using the same MCMC model as above, a good agreement is obtained between the spectrum and the model when the area is ~150 km^2 and the temperature is T = 640 ± 60 K (Figure 2 panel A). The feature is found to emit the considerable power P = 1.40 ± 0.17 TW; uncertainties on T and P are 1σ.

A.2 Scaling Volcanic Structures on Io to the Earth

The simultaneous or near simultaneous eruptions across arc distances of 800 km on Io suggests several possible origins. The eruptive centers could be distinct and unconnected, but responsive to a broad influx of magma from Io’s tidally heated mantle, in the manner of large igneous provinces (LIPs) on Earth. On Earth, however, LIPs are widely thought due the arrival of mantle plume heads arising from great depths (e.g., Mittal et al., 2021), which is a very unlikely scenario for Io’s strongly internal tidally heated mantle. There is also the matter of scale. Given the basic similarity of rock and magma densities on Earth and Io, dynamic scaling suggests that volcanic structures on Io arising from similar mechanisms as on Earth will size-scale as the inverse ratio of their surface gravities, or by a factor of ~5.5. Therefore, the 200-400 km distances between the main feature A and the active outlying features on Io could correspond to separation distances between eruptive centers on Earth of ~35-75 km. This is an interesting distance range with respect to volcanic interactions on Earth, and corresponds to the transition between stress or pressure change coupling and that due to anomalously large magmatic or tectonic events (Biggs et al., 2016). Also, such a scale on Earth (~50 km) is much smaller than the horizontal extent of LIPs, but more similar to that within intraplate volcanic edifices (as described below). Magmatic connections on Earth can also exist over similar distances within midocean ridge segments (Goss et al., 2010; Tan et al., 2016) and potentially over even greater distances (>100 km) when the tectonic environment is favorable, such as at propagating midocean rifts (Kahle et al., 2016).

A.3 Post-event monitoring and decay timescale

Following the event observed during Juno's orbit 68, the JIRAM instrument was pointed again toward the region affected by the eruption in the following orbits. At the time, Juno was in a resonant orbit with Io, specifically designed so that every two Juno orbits would provide a good opportunity for JIRAM to observe Io.

Given the event's intensity, during the next two observations (Juno orbits 70 and 72), the JIRAM exposure times were kept extremely short to avoid signal saturation, which was successfully achieved (see Figure 1, panels E and F). This allowed for a reliable estimation of the spectral total power in the M and L bands during those two subsequent orbits. The retrieved values are, for the M band: P_{M70} = 0.9 TW μm^{-1} and P_{M72} = 0.7 TW μm^{-1}; for the L band: P_{L70} = 0.3 TW μm^{-1} and P_{L72} = 0.17 TW μm^{-1}. These measurements indicate that total power decreased with a ~20-day characteristic timescale during the first two months after the event, with a slower decline observed in the following period. The characteristic of the flow is discussed in Lopes et al. (2025).

References

Adriani, A., Filacchione, G., Di Iorio, T. et al., 2017. JIRAM, the Jovian Infrared Auroral Mapper, Space Science Reviews, 213(1–4), pp. 393–446. https://doi.org/10.1007/s11214-014-0094-y.

Adriani, A. 2019. Juno JIRAM Bundle, [Dataset] PDS Atmospheres (ATM) Node, https://doi.org/10.17189/1518967.

Becker, H. N., Schenk, P. M., Lopes, R. M. C., Brennan, M. J., Florence, M. M., Mura, A., et al., 2025. Channelized thermal emission, Promethean-type jets and surface changes on Io from Juno Stellar Reference Unit imagery. Journal of Geophysical Research: Planets, 130, e2024JE008744. https://doi.org/10.1029/2024JE008744

Biasi, J. and Karlstrom, L., 2021. Timescales of magma transport in the Columbia River flood basalts, determined by paleomagnetic data. Earth and Planetary Science Letters, 576, p.117169.

Biggs, J., Elspeth Robertson, E.R., and Cashman, K. (2016) The lateral extent of volcanic interactions during unrest and eruption. Nature Geoscience 9, 308–311, doi: 10.1038/NGEO2658.

Bland, M.T., McKinnon, W.B., 2016. Mountain building on Io driven by deep faulting. Nat. Geosci. 9, 429–432.

Burgess, M. K., & Roman, D. C., 2021. Ongoing (2015-) magma surge in the upper mantle beneath the Island of Hawaiʻi. Geophysical Research Letters, 48, e2020GL091096. https://doi.org/10.1029/2020GL091096

Carr, M.H., Masursky, H., Strom, R.G., Terrile, R.J., 1979. Volcanic features of Io. Nature. 280, 729–733

Carr, M.H., McEwen, A.S., Howard, K.A., et al., 1998. Mountains and Calderas on Io: Possible Implications for Lithosphere Structure and Magma Generation. Icarus 135, 146. https://doi.org/10.1006/icar.1998.5979

Eibl, E.P., Bean, C.J., Vogfjörd, K.S., Ying, Y., Lokmer, I., Möllhoff, M., O'Brien, G.S. and Pálsson, F., 2017. Tremor-rich shallow dyke formation followed by silent magma flow at Bárðarbunga in Iceland. Nature Geoscience, 10(4), pp.299-304.

Goss, A. R., M. R. Perfit, W. I. Ridley, K. H. Rubin, G. D. Kamenov, S. A. Soule, A. Fundis, and D. J. Fornari (2010), Geochemistry of lavas from the 2005–2006 eruption at the East Pacific Rise, 9°46′N–9°56′N: Implications for ridge crestplumbing and decadal changes in magma chamber compositions, Geochem. Geophys. Geosyst., 11, Q05T09, doi:10.1029/2009GC002977

Hamilton, C.W., Beggan, C.D., Still, et al., 2013. Spatial distribution of volcanoes on Io: Implications for tidal heating and magma ascent. Earth and Planetary Science Letters, 361, pp.272-286.

Jaeger, W.L., Turtle, E.P., Keszthelyi, L.P., et al., 2003. Orogenic tectonism on Io. Journal of Geophysical Research: Planets, 108(E8).

Jellinek, A.M. and DePaolo, D.J., 2003. A model for the origin of large silicic magma chambers: precursors of caldera-forming eruptions. *Bulletin of Volcanology*, *65*, pp.363-381.

Karlstrom, L., Dufek, J. and Manga, M., 2009. Organization of volcanic plumbing through magmatic lensing by magma chambers and volcanic loads. Journal of Geophysical Research: Solid Earth, 114(B10).

Karlstrom, L., Paterson, S.R. and Jellinek, A.M., 2017. A reverse energy cascade for crustal magma transport. Nature Geoscience, 10(8), pp.604-608.

Kahle, Richard L., Frederik Tilmann, and Ingo Grevemeyer. Crustal structure and kinematics of the TAMMAR propagating rift system on the Mid-Atlantic Ridge from seismic refraction and satellite altimetry gravity, Geophys. J. Int. (2016) 206, 1382–1397. doi: 10.1093/gji/ggw219.

de Kleer, K., de Pater, I., 2017. Io's Loki Patera: modeling of three brightening events in 2013-2016. Icarus 289, 181–198.

de Kleer, K., Nimmo, F. and Kite, E., 2019a. Variability in Io's volcanism on timescales of periodic orbital changes. Geophysical Research Letters, 46(12), pp.6327-6332.

de Kleer, Katherine, et al., 2019b. Tidal heating: Lessons from Io and the Jovian system-final report." Keck Institute for Space Studies. https://doi.org/10.26206/d4wc-6v82.

Keszthelyi, L., Jaeger, W.L., Turtle, E.P., Milazzo, M., Radebaugh, J., 2004. A post-Galileo view of Io's interior. Icarus 169, 271–286.

Leone, G., A.G. Davies, L. Wilson, D.A. Williams, L.P. Keszthelyi, W.L. Jaeger, E.P. Turtle, 2009. Volcanic history, geologic analysis and map of the Prometheus Patera region on Io. J. Volcan. Geotherm. Res. 187, 93–105.

Lopes, R.M.C. et al., 2004. Lava lakes on Io: observations of Io's volcanic activity from Galileo NIMS during the 2001 fly-bys, Icarus, 169(1), pp. 140–174.

Lopes, R. M. C., Mura, A., Mouginis-Mark, P., Radebaugh, J., Tosi, F., Zambon, F., et al. (2025). Thermal characteristics of active lava flows on Io observed by the JIRAM instrument on Juno. Journal of Geophysical Research: Planets, 130, e2025JE008940. https://doi. org/10.1029/2025JE008940

Marchis, F., I. de Pater, A.G. Davies, H.G. Roe , T. Fusco, D.Le Mignant, P. Descamps, B.A. Macintosh, R. Prangé, 2002. High-Resolution Keck Adaptive Optics Imaging of Violent Volcanic Activity on Io. Icarus. 160 (1): 124–131.

McEwen AS, Keszthelyi L, Spencer JR, Schubert G, Matson DL, Lopes-Gautier R, Klaasen KP, Johnson TV, Head JW, Geissler P, Fagents S, Davies AG, Carr MH, Breneman

HH, Belton MJ, 1998. High-temperature silicate volcanism on Jupiter's moon Io. Science, 281(5373):87-90. doi: 10.1126/science.281.5373.87. PMID: 9651251.

McEwen, A.S., Belton, M.J.S., Breneman, H.H., Fagents, S.A., Geissler, P., Greeley, R., Head, J. W., Hoppa, G., Jaeger, W.L., Johnson, T.V., Keszthelyi, L., 2000. Galileo at Io: results from high-resolution imaging. Science 288, 1193 – 1198.

McEwen, A.S., Haapala, A.F., Keszthelyi, L.P., Mandt, K.E., 2023. "Outstanding Questions and Future Observations of Io" in: Io: A New View of Jupiter's Moon. Astrophysics and Space Science Library, Vol. 468. ISBN: 978-3-031-25670-7. New York, NY: Springer New York, 2023, pp. 349-370

Mittal, T., Richards, M. A., & Fendley, I. M. (2021). The magmatic architecture of continental flood basalts I: Observations from the Deccan Traps. Journal of Geophysical Research: Solid Earth, 126, e2021JB021808. https://doi. org/10.1029/2021JB021808.

Montagna, C.P. and Gonnermann, H.M., 2013. Magma flow between summit and Pu ‘u ‘Ō ‘ō at K̄lauea Volcano, Hawai ‘i. Geochemistry, Geophysics, Geosystems, 14(7), pp.2232-2246.

Mura, A., Adriani, A., Tosi, F., Lopes, R. M. C., Sindoni, G., Filacchione, G., et al. (2020). Infrared observations of Io from Juno. Icarus, 341, 113607. https://doi.org/10.1016/j.icarus.2019.113607

Mura A, Zambon F, Tosi F., et al., 2024a. The temporal variability of Io’s hotspots. Front. Astron. Space Sci. 11:1369472. doi: 10.3389/fspas.2024.1369472

Mura, A., Tosi, F., Zambon, F., et al., 2024b. Hot rings on Io observed by Juno/JIRAM. Commun Earth Environ 5, 340. https://doi.org/10.1038/s43247-024-01486-5

Mura, A., Tosi, F., Zambon, F., et al. (2025a). Widespread occurrence of lava lakes on Io observed from Juno. Journal of Geophysical Research: Planets, 130, e2024JE008723.

Mura, A. R. M. C. Lopes, F. Tosi, et al, (2025b). Observations of Loki Patera by Juno during Close Flybys, The Planetary Science Journal, Volume 6, Number 2, DOI 10.3847/PSJ/ada27c

Mura, A. (2025c). Dataset and code for the research article "Synchronized Eruptions on Io: Possible Evidence of Interconnected Subsurface Magma Reservoirs" [Data set]. Zenodo. https://doi.org/10.5281/zenodo.17523325

O’Reilly, T.C., Davies, G.F., 1981. Magma transport of heat on Io: a mechanism allowing a thick lithosphere. Geophys. Res. Lett. 8, 313–316. https://doi.org/10.1029/GL008i004p00313

Park, R.S., Jacobson, R.A., Gomez Casajus, L. et al., 2025. Io’s tidal response precludes a shallow magma ocean. Nature. https://doi.org/10.1038/s41586-024-08442-5

Pettine, M., Imbeah, S., Rathbun, J., Hayes, A., Lopes, R. M. C., Mura, A., et al., 2024. JIRAM observations of volcanic flux on Io: Distribution and comparison to tidal heat flow models. Geophysical Research Letters, 51, e2023GL105782. https://doi.org/10.1029/2023GL105782

Poland, M.P., Miklius, A., Jeff Sutton, A. and Thornber, C.R., 2012. A mantle-driven surge in magma supply to Kīlauea Volcano during 2003–2007. Nature Geoscience, 5(4), pp.295-300.

Radebaugh, J., Keszthelyi, L.P., McEwen, A.S., Turtle, E.P., Jaeger, W., Milazzo, M., 2001. Patera on Io: A new type of volcanic caldera? J. Geophys. Res. 106, 33,005 – 33,020.

Radebaugh, J., McEwen, A.S., Milazzo, et al., 2004. Observations and temperatures of Io's Pele Patera from Cassini and Galileo spacecraft images. Icarus, 169(1), pp.65-79.

Reidel, Stephen P., Victor E. Camp, Terry L. Tolan, Barton S. Martin, 2013. "The Columbia River flood basalt province: Stratigraphy, areal extent, volume, and physical volcanology", The Columbia River Flood Basalt Province, Stephen P. Reidel, Victor E. Camp, Martin E. Ross, John A. Wolff, Barton S. Martin, Terry L. Tolan, Ray E. Wells

Schenk, P., Hargitai, H., Wilson, R., McEwen, A. and Thomas, P., 2001. The mountains of Io: Global and geological perspectives from Voyager and Galileo. Journal of Geophysical Research: Planets, 106(E12), pp.33201-33222.

Spencer, D.C., Katz, R.F., Hewitt, I.J., 2020. Magmatic intrusions control Io’s crustal thickness. J. Geophys. Res. Planets. 125.

Tan, Yen Joe, Maya Tolstoy, Felix Waldhauser1 & William S. D. Wilcock. (2016) Dynamics of a seafloor-spreading episode at the East Pacific Rise. Nature 540, 261-265. doi:10.1038/nature20116.

Tosi, F., et al., 2025. Re-evaluating Io's Volcanic Heat Flow: Critical Limitations in Juno/JIRAM M-band Analysis, Front. Astron. Space Sci., 05 November 2025, Sec. Planetary Science, Volume 12, doi.org/10.3389/fspas.2025.1668185

Turtle, E.P., Jaeger, W.L., Keszthelyi, L.P., et al., 2001. Mountains on Io: High-resolution Galileo observations, initial interpretations, and formation models. Journal of Geophysical Research: Planets, 106(E12), pp.33175-33199.

Turtle, E.P., et al. 2004. The final Galileo SSI observations of Io: orbits G28-I33, Icarus 169, 3 – 28.

Veeder, G.J., Davies, A.G., Matson, D.L., Johnson, T.V., Williams, D.A., Radebaugh, J., 2015. Io: heat flow from small volcanic features. Icarus 245, 379–410. https://doi.org/10.1016/j.icarus.2014.07.028.

Veeder, G.J., Davies, A.G., Matson, D.L., Johnson, T.V., Williams, D.A., Radebaugh, J., 2012. Io: volcanic thermal sources and global heat flow. Icarus 219, 701–722. https://doi.org/10.1016/j.icarus.2012.04.004.

Wilding J.D. et al., 2023. The magmatic web beneath Hawai‘i. Science 379, 462-468. doi:10.1126/science.ade5755

Williams, D.A., Keszthelyi, L.P., Crown, et al. (2011a). Volcanism on Io: New insights from global geologic mapping. Icarus 214, 91 - 112. doi.org/10.1016/j.icarus.2011.05.007

Williams, D.A., Keszthelyi, L.P., Crown, et al. (2011b), Geologic map of Io: U.S. Geological Survey Scientific Investigations Map 3168, scale 1:15,000,000, 25 p., available at https://pubs.usgs.gov/sim/3168/.

Open Research

The data used in this study comes from Juno and the Jovian Infrared Auroral Mapper (JIRAM) and is publicly available on the Planetary Database System in PDS4 format (Adriani et al., 2019). The SPICE bundles used to calibrate the viewing geometry are also publicly available in the Planetary Database System via the Navigation and Ancillary Information Facility (NAIF). The code for the MCMC model is provided via Mura et al. (2025c). The Voyager-Galileo Io data used for our analysis is available through Williams et al., (2011a) on the U.S. Geological Survey Scientific Investigations website (Williams et al., 2011b).

Acknowledgments

We thank Agenzia Spaziale Italiana (ASI) for the support of the JIRAM contribution to the Juno mission. This work is funded by the ASI–INAF Addendum n. 2016-23-H.3-2023 to grant 2016-23-H.0. Part of this work was performed at the Jet Propulsion Laboratory, California Institute of Technology, under contract with NASA.

Corresponding author

Correspondence to Alessandro Mura (alessandro.mura@inaf.it)

Competing interests

The authors declare no competing interests.

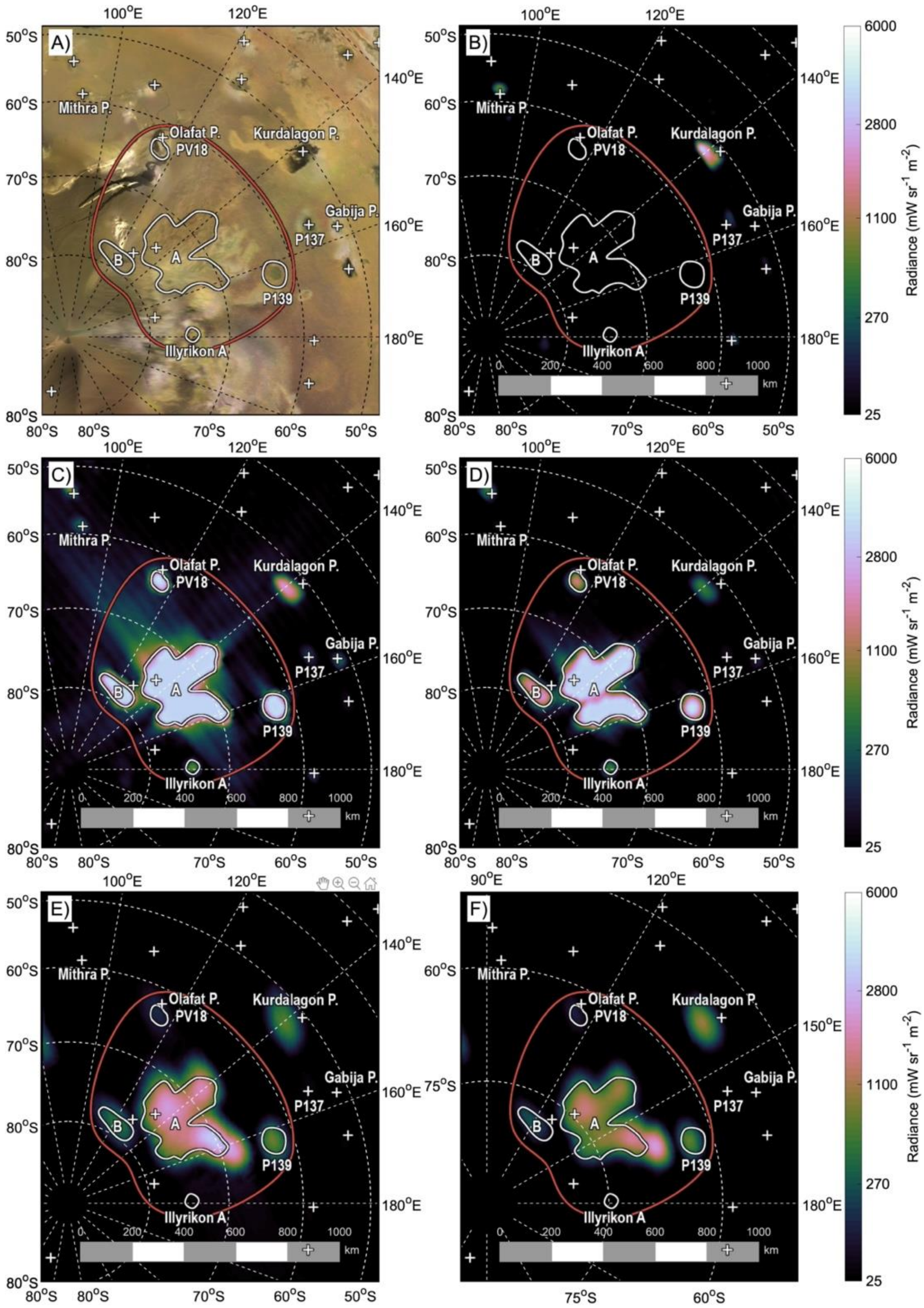

Figure 1. Panel A: USGS map of the region of interest (Williams et al., 2011); Panel B: band radiance map in the M band, from JIRAM, taken during orbit 66 (PJ 66; Oct. 22, 2024); Panel C: same, observed during orbit 68 (PJ 68; Dec. 27, 2024); Panel D: same, for L-band data. Panels E and F: M-band maps for orbits 70 and 72. Location of some previously known hot spots are indicated by white crosses or white contours. M-band radiance is integrated from ~4.5 to 5 µm; L-band radiance is integrated from ~3.3 to 3.6 µm. The color scale is not linear to enhance the retails at low radiance; white is saturated. In PJ 66, only Kurdalagon P. shows a significant radiance, and P137 is barely visible at a similar radiance as in PJ 68. PV18 P., P139, the unnamed feature at 80°S, 120°E and Illyrikon A. are completely dark in PJ 66 but visible in PJ 68. The region that encompasses the locations that erupted simultaneously, as observed in PJ 68, is drawn in red.

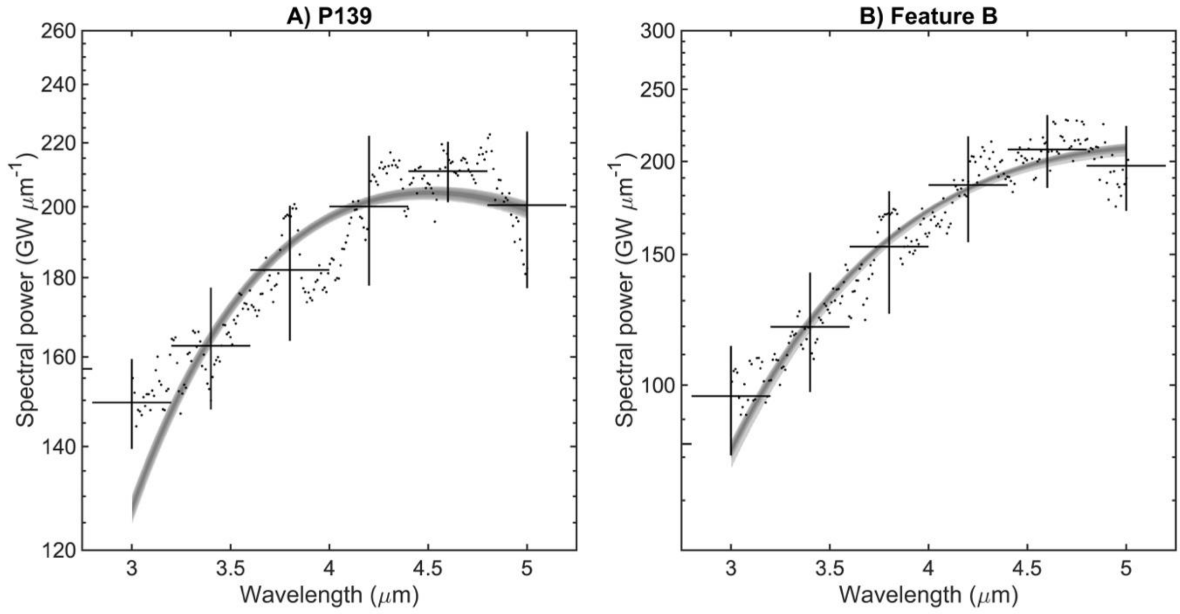

Figure 2. Panel A: Spectral power from P139 and MCMC model. Dots are data, sampled at 9 nm spectral resolution; crosses are averages over 0,25 µm; gray lines are the MCMC model (increasing shades of gray show decreasing confidence levels: 95%, 90% and 75%). Panel B, same for Feature B. P139 has a model temperature of 640K ± 60 K (1-σ uncertainty), Feature B has a model temperature of 550 K ± 50 K (1-σ uncertainty).

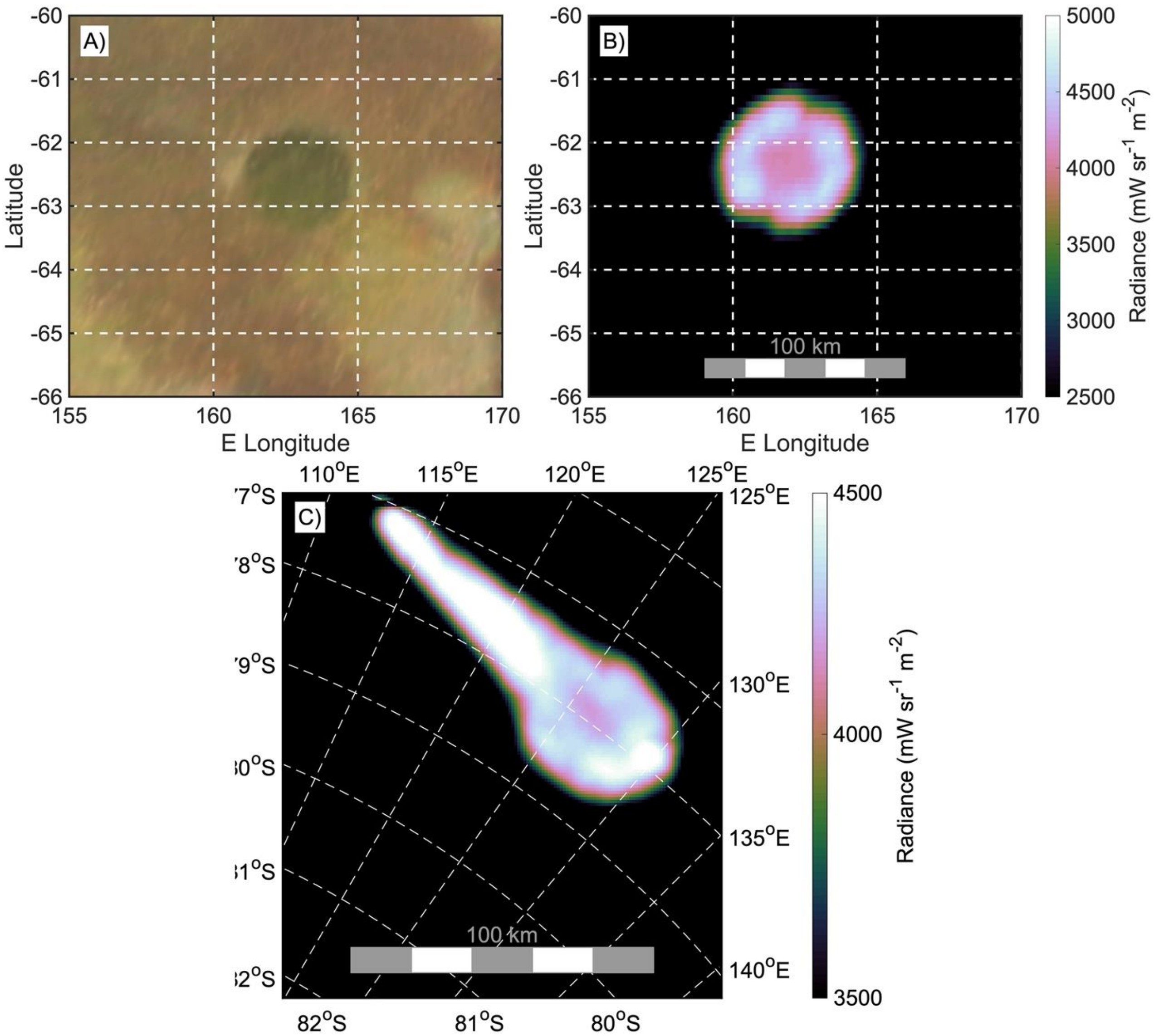

Figure 3. Panels A and B: maps of P139 in the visible and in the infrared, respectively. M-band radiance map is integrated from 4.5 to 5 µm. The IR map clearly shows a ring-shaped emission, typical of lava lakes. The projection is cylindrical equirectangular. Panel C: Feature B with a stretched color-scale in a polar projection (there is no useful visible counterpart of this region).

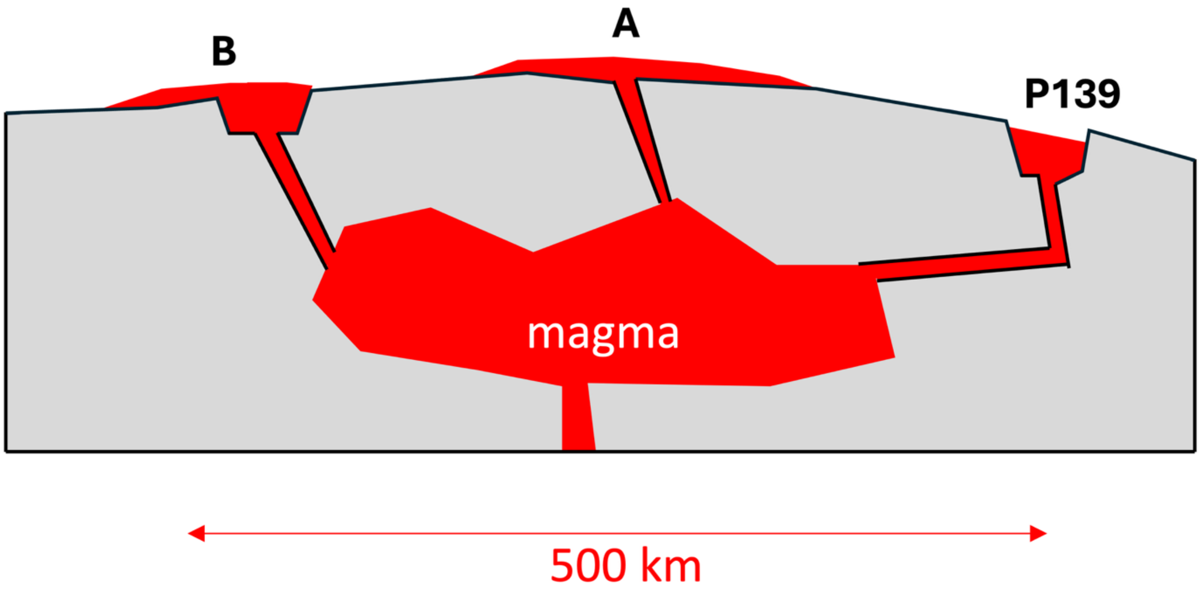

Figure 4: Conceptual cross-section showing the proposed subsurface magma chamber system. A large, interconnected magma reservoir (red) feeds surface eruptions at Features A, B, and P139. Horizontal scale approximately 500 km; vertical scale not to scale.

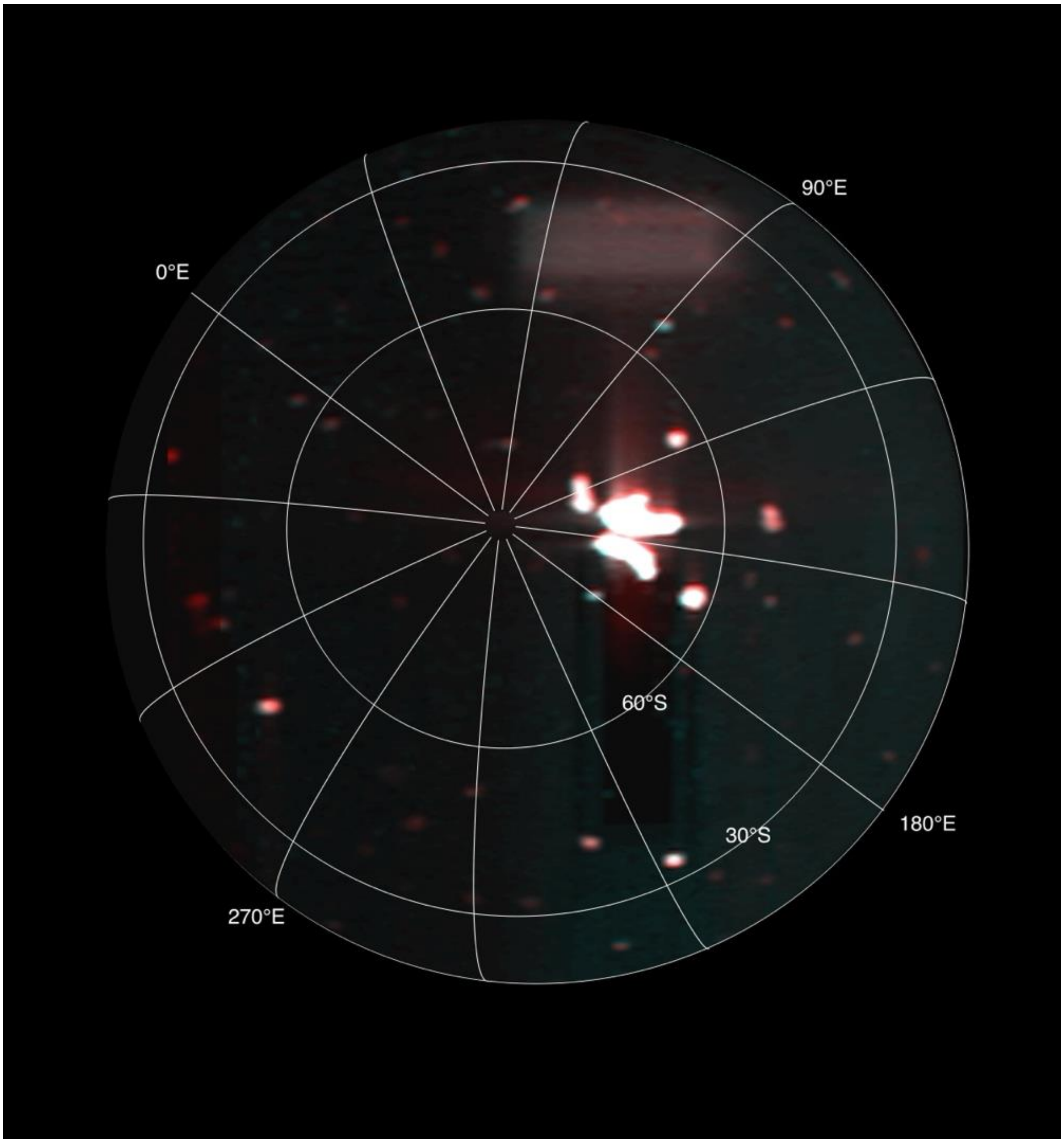

Fig. A1. Raw data from JIRAM, taken on Dec. 27, 2024, from a distance of ~100,000 km (unprocessed data). The spacecraft was looking at the south pole of Io; the extreme event feature is clearly visible to the right of the pole; a rectangular feature above is due to stray-light. Meridians and parallels (steps of 30°) are overlayed on the data.

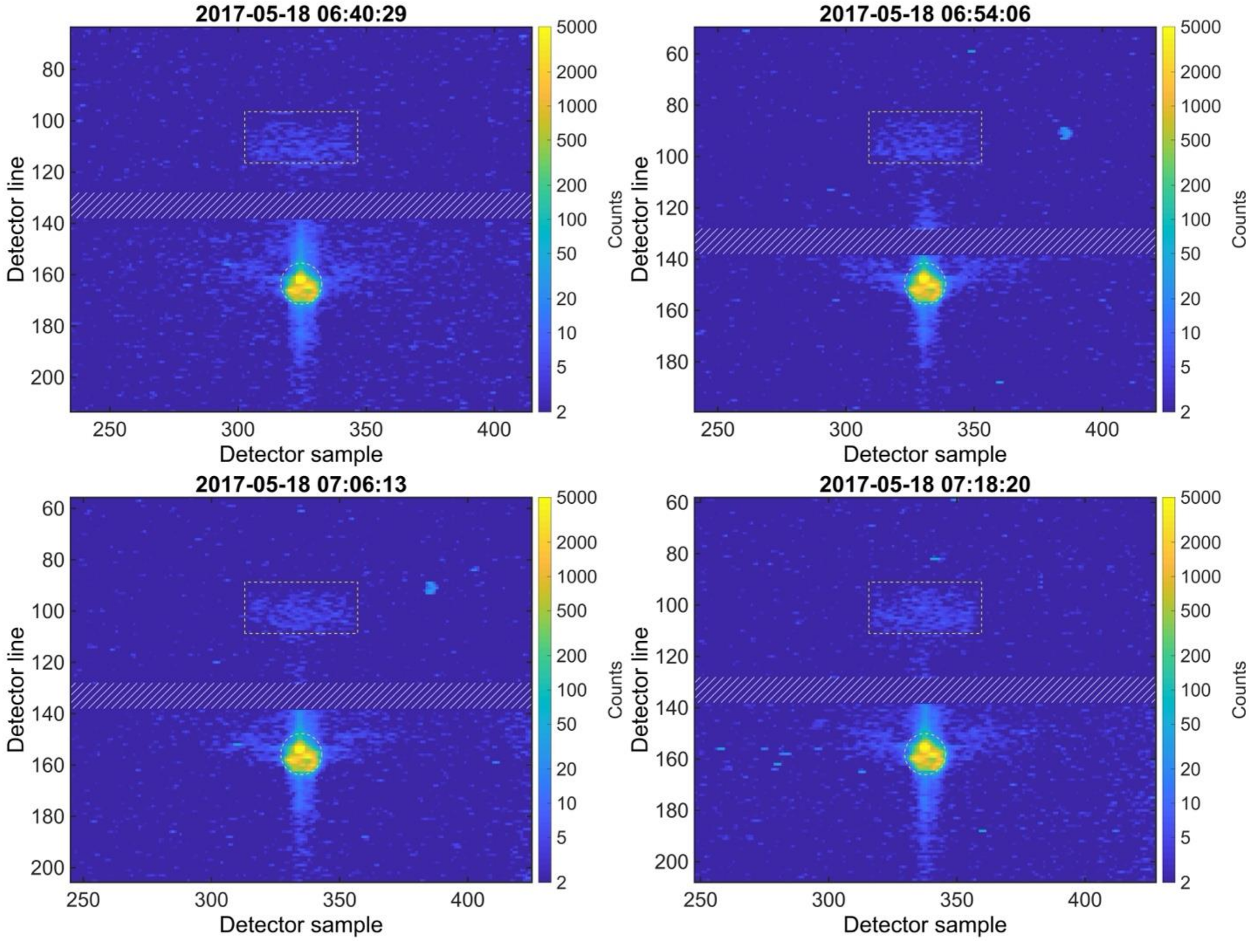

Fig. A2. Io as seen in orbit 6 (in the M band, in the white circle), and the stray-light feature (in the white rectangle). Four examples are given at different times, showing the stability of the feature.

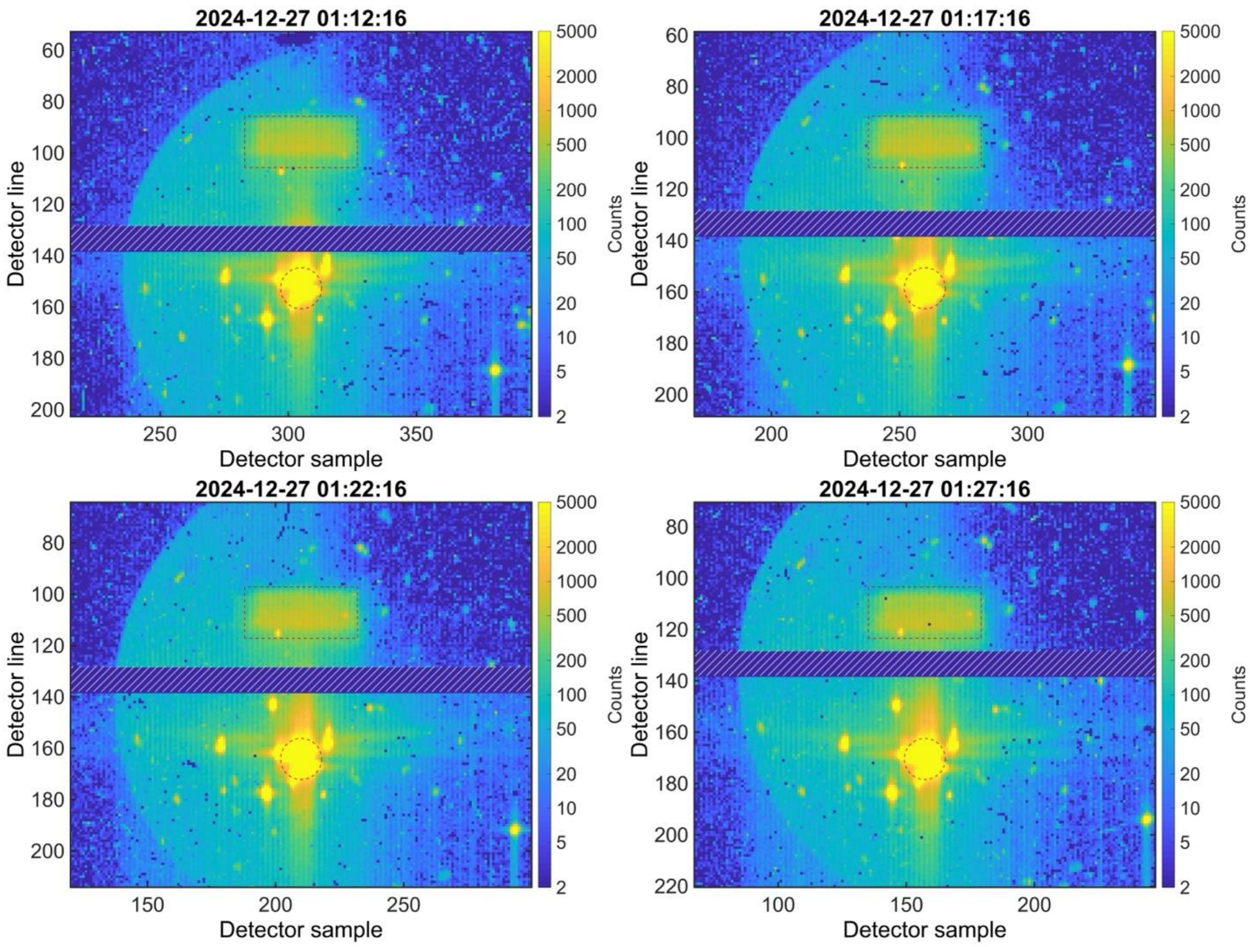

Fig. A3. Same as Figure A2, for orbit 68. In this case, the signal in the circle is emitted from the feature "A" and produces the stray-light signal inside the rectangle.

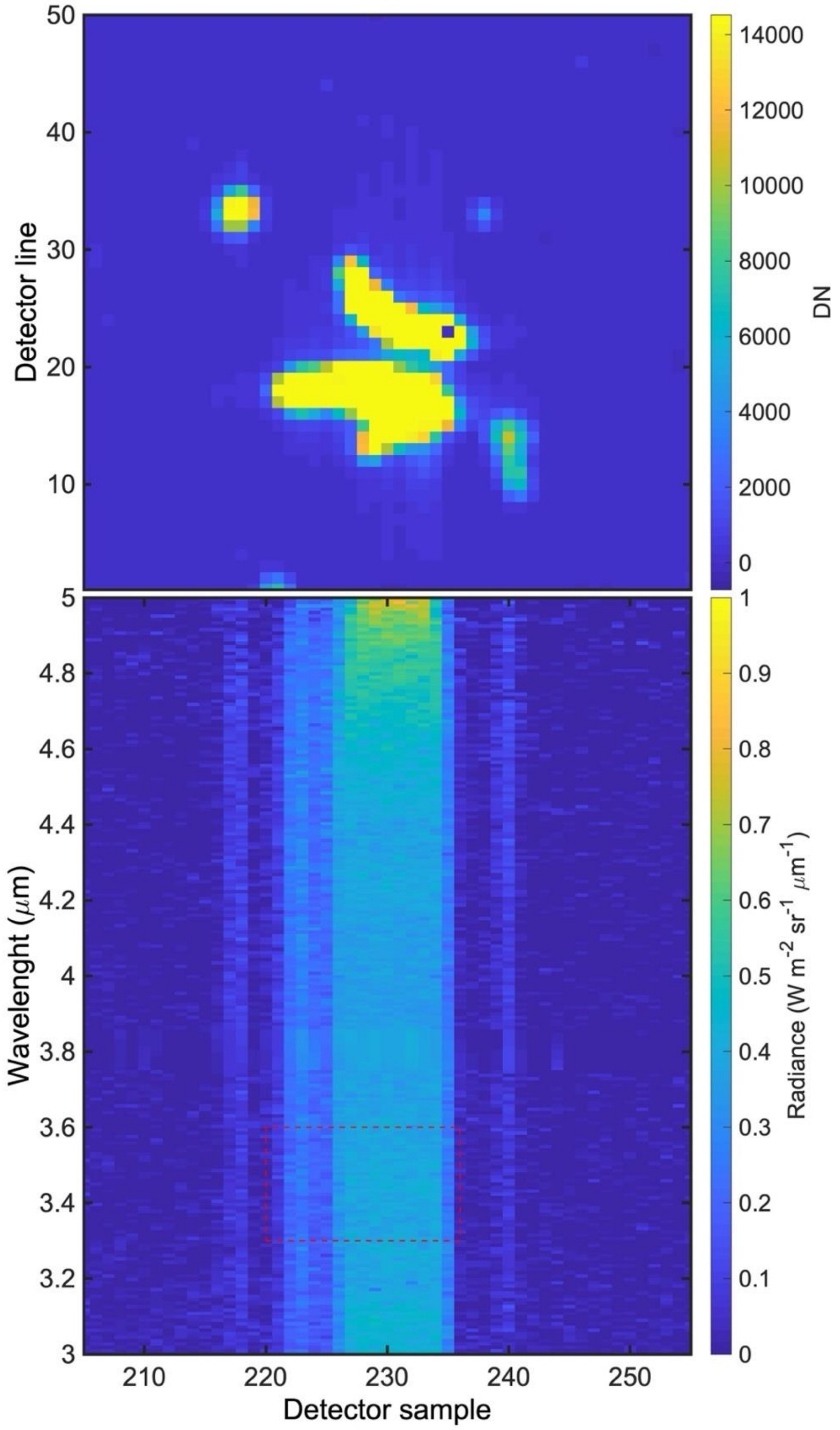

Fig. A4. Top: imager raw data (L band), showing the feature "A" between samples 221 and 236. Bottom: spectrometer calibrated data from 3 to 5 μm. The rectangle corresponds to samples from 221 to 236 and to wavelengths from 3.3 to 3.6 μm.

Feature	PJ66			PJ68				
	P_L GW μm^{-1}	P_M GW μm^{-1}	P TW	P_L GW μm^{-1}	P_M GW μm^{-1}	P TW	T K	Area km^2
A	n/a [a]	n/a [a]	0.100 [c]	8.9 10^3	19 10^3	200 ± 60	500 ± 50	65000
B	n/a [a]	n/a [a]		>40	>100	1.7 ± 0.2 [b]	550 ± 50	300
PV18	n/a [a]	0.35	0.09 [d]	40	80	~1	~500	300
P139	n/a [a]	0.05	<0.08 [e]	140[f]	200 [f]	1.40±0.17 [b]	640 ± 60	150
Illyrikon A	0.15	0.2	0.0015	10	7	0.05	~900	n/a [g]

Table 1. Spectral power, total power, retrieved temperature and area for 5 features discussed in this study. [a] no signal detected above the background level (median of the signal outside any feature), which is 2.5 mW m^{-2} sr^{-1}. [b] imager is saturated; total power is obtained with a MCMC model on the spectrometer data; uncertainty on the temperature is 1σ. [c] based on our reanalysis of PPR data. [d] from literature, Veeder et al. (2015). [e] based on P_M only, and assuming any temperature > 200 K. [f] based on the spectrometer. [g] area too small (a few km^2) for reliable retrieval.

UTC (27-12-2024)	R $W \cdot m^{-2}\,sr^{-1}\,\mu m^{-1}$	R' $W \cdot m^{-2}\,sr^{-1}\,\mu m^{-1}$	Distance 1000 km	P_M $TW\,\mu m^{-1}$
00:57:45	0.1418	57	99	20
01:02:45	0.1629	65	94	20
01:12:16	0.2007	80	85	21
01:17:16	0.2190	88	81	21
01:22:16	0.2249	90	79	20
01:27:16	0.2182	87	77	19
01:32:16	0.2156	86	76	18
01:37:16	0.1840	74	77	15
Average	**0.20 ± 0.06**	**78 ± 25**	**83**	**19 ± 4**

Table A1 Data for the calculation in section A.1.1, for the M-band data, not including the uncertainty on the scaling factor. Note that the average value for P_M is calculated as the average of the value in the last column, not from the multiplication of the average R', etc., but the result is the same.

UTC (27-12-2024)	R $W \cdot m^{-2} sr^{-1} \mu m^{-1}$	R' $W \cdot m^{-2} sr^{-1} \mu m^{-1}$	Distance 1000 km	P_L TW μm^{-1}
01:01:15	0.2385	30	95	9.7000
01:01:45	0.2284	29	95	9.2000
01:06:15	0.2644	33	90	9.6000
01:06:45	0.2529	32	90	9.1000
01:11:16	0.2947	37	86	9.7000
01:11:46	0.2808	35	85	9.2000
01:16:46	0.3068	38	82	9.2000
01:21:46	0.3226	40	79	9.0000
01:26:16	0.3524	44	77	9.4000
01:26:46	0.3218	40	77	8.6000
01:31:16	0.3187	40	76	8.3000
01:31:46	0.3045	38	76	7.9000
01:36:16	0.2846	36	76	7.4000
Average	**0.29 ± 0.08**	**36 ± 10**	**83**	**8.9 ± 1.4**

Table A2. Same as Table A1; data for the calculation in section A.1.1, for the L-band data.